Supplementary information

CALCULATION PARAMETERS

In order to determine the ground state properties of the negatively charged boron vacancy in 2D hBN we perform DFT calculations using the PBE exchange-correlation functional on a 8x8 supercell with the open-source Quantum ESPRESSO distribution [1]. The planewave cutoff used is 80 Ry and the Brillouin zone is sampled with a 2x2x1 unshifted grid. The norm-conserving pseudopotential adopted for boron and nitrogen are taken from the PseudoDojo library [2].

We correct the Kohn-Sham eigenvalues with a G_0W_0 calculation under the plasmon pole approximation, using the Yambo code [3, 4]. We use 5 Ry and 19 Ry cutoff respectively for the response function and the exchange self energy, and sum 2000 bands both for the response function and the correlation self-energy. We sample the Brillouin zone with a 2x2x1 unshifted grid. We checked the results by performing the same calculations on a 10x10 supercell, sampling the Brillouin zone with a gamma-only grid, summing 3000 bands both for the response functions and the correlation self-energy and using 4 Ry and 15 Ry cutoff respectively for the response function and the exchange self energy.

The absorption spectrum is determined by solving the equilibrium Bethe-Saltpeter equation (BSE), using 2 Ry cutoff for the electron-hole attraction part of the kernel, 9 Ry cutoff for the exchange part of the kernel and bands from 190 to 320 (whose energy is corrected using the G_0W_0 approximation). The FFT grid is reduced to 21 Ry. Results were The phonon-assisted luminescence calculations converge when considering bands from 251-256, thanks to the effect of the nonequilibrium occupations.

The phonons are calculated in Γ with the finite-difference approach, using the code Phonopy [5].

ABSORPTION

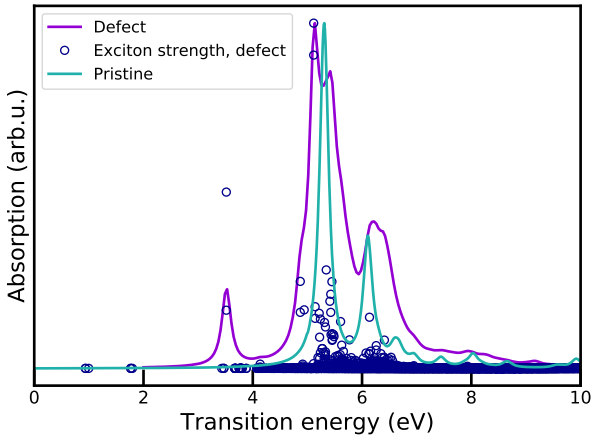

FIG. 1: Absorption spectrum for V_B^- center in 2D hBN (purple line) and for the pristine 2D hBN (light blue line). The blue circles represent the strength of the excitons of the defected system as a function of their energy.

The absorption spectrum is shown in Fig. 1. Here we perform an analyisis similar to that done in Ref. [6] for the absorption spectrum of the neutral defects in 2D hBN. The strong peak at 5.3 eV which dominates the pristine spectrum, is splitted into two subpeaks at 5.15 eV and 5.40 eV by the resonant coupling of transitions between the extended conduction and valence states with the defect states close to the band edges.

The transition between the spin down level a_1' and the spin down level e' (see Fig. 4a of the main text), which is associated to a non vanishing in-plane dipole, leads to a bright peak at 3.5 eV. The shoulder at 4.85 eV arises due to the mixing of the transitions from the defect levels to the conduction band and the bulk excitations.

The excitons at 0.94 eV and 1.77 eV do not contribute appreciably to the absorption spectrum because are localised on the transitions $e'' \rightarrow e'$, which has a non-vanishing out-of-plane dipole and therefore is very weak in an atomically thin material, and $a_2'' \rightarrow e'$, which is prohibited by symmetry.

EFFECT OF NONEQUILIBRIUM OCCUPATION

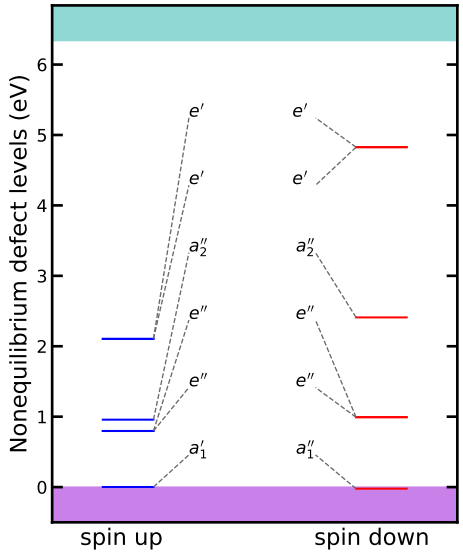

FIG. 2: Nonequilibrium energy levels

FIG. 3: Defect energy levels renormalized by the nonequilibrium occupations of Fig. 4a of the main text.

As stated in the main text, if the excited state dynamics continues for long enough, it is reasonable to assume that both electron and holes thermalise. In the current work, we set the chemical potential for the electrons in such a way that a whole electron is promoted to the excited state manifold, consistently with what is done in works based on quantum chemistry techniques or cDFT [7]. This corresponds to an excited carrier density of 2.5×10^{13} electrons per cm^2. The temperature of electrons and holes is assumed to be equal to that of the phonon bath with which they interact. The chemical potential of the holes is tuned in such a way that the number of holes coincides with that of the electrons excited in the conduction band. This assumes the excitations in photoluminescence experiments are neutral.
The nonequilibrium occupations induce a renormalization of the quasiparticle energy levels. The renormalized energies are calculated in Yambo as:

$$\varepsilon_{NEQ} = \varepsilon^{G0W0}_{EQ} + (\varepsilon^{COHSEX}_{NEQ} - \varepsilon^{COHSEX}_{EQ})\,; \tag{1}$$

The first therm in the r.h.s. is the quasiparticle energy determined at the G_0W_0 level of theory using the equilibrium occupations (Fig. 4a of the main paper), while the second and

the third term represent the quasiparticle energy at the COHSEX level of theory calculated using the nonequilibrium and equilibrium occupations respectively. As it can be observed when comparing Fig. 2 with Fig. 4a of the main paper, the nonequilibrium occupations lead to a downshift of the spin down level e' which is occupied by excited electrons, and a upshift of the spin levels e'' and a_2'' which are occupied by holes.

As discussed in the main work, the only transition where both levels have non-negligible population in term of electrons and holes is the (spin down) $e' \rightarrow a''$. Therefore it is interesting to see how this transition is distributed among the excitons, both at equilibrium and at nonequilibrium, by plotting

$$T_K(\omega) = \sum_\lambda |A_K^\lambda|^2 \delta(\omega - E_\lambda) \tag{2}$$

for $K \equiv e' \rightarrow a_2''$. As it is possible to observe in Fig. 4, at equilibrium this transition is mainly localised in exciton of energy 0.94 eV and 1.77 eV. When an integer amount of charge is excited, so that the nonequilibrium occupations differ from the equilibrium ones, the transition $e' \rightarrow a_2''$ localises on two excitons of energy 1.4 eV and 1.5 eV. It is instructive,

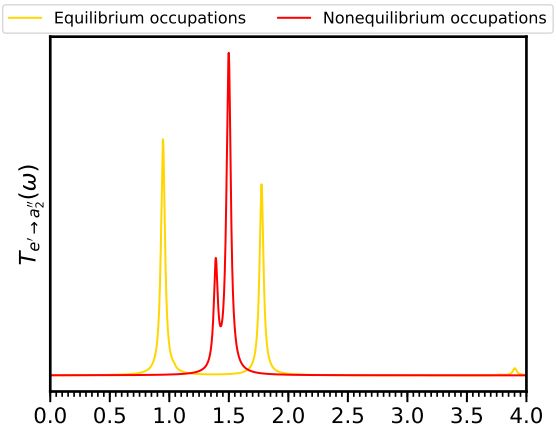

FIG. 4: Distribution of the transition $e' \rightarrow a_2''$ among the excitons, both at equilibrium and out of equilibrium.

finally, to plot the phonon-assisted photoluminescence and the exciton-phonon coupling in the equilibrium occupations case for the exciton at 1.77 eV (see Fig. 5). Interestingly, the modes which couple the most strongly with excitons are the same, leading to a similar luminescence spectrum. The exciton-phonon coupling is now symmetric, due to the absence of a excitonic shoulder at lower energy.

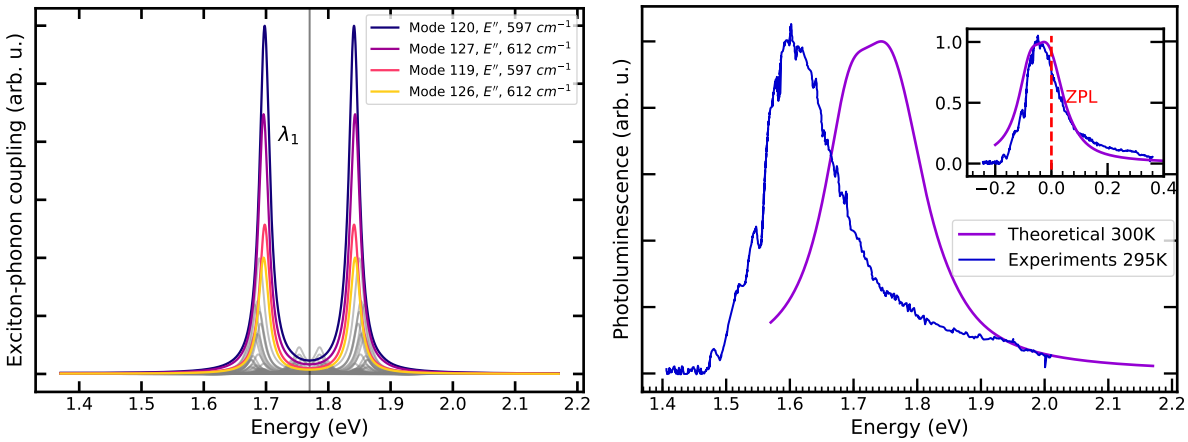

(a) Exciton-phonon coupling

(b) Luminescence spectrum

FIG. 5: Panel (a) shows the exciton-phonon coupling function in the case of equilibrium occupations (very low excited charge) for the exciton at 1.77 eV, while panel (b) shows the luminescence spectrum.

PHONON CALCULATIONS

As anticipated in the first section, phonons are calculated at the Γ point only using a finite-difference approach. The other points of the Brillouin zone are not considered in the exciton-phonon coupling calculations, as they are characterized by a periodicity which is unphysical for a defect center. The 8x8 supercell contains 127 atoms, leading to 381 phonon modes, whose frequencies range from 0 to around 1500 cm^{-1}. Due to numerical noise in the calculations, 7 membrane modes have slightly negative frequencies, and are not included in the exciton-phonon coupling calculations.

It is interesting to analyze the localization of the phonon modes around the defect centers. With this purpose, we calculate a localization factor defined as the sum of the squared

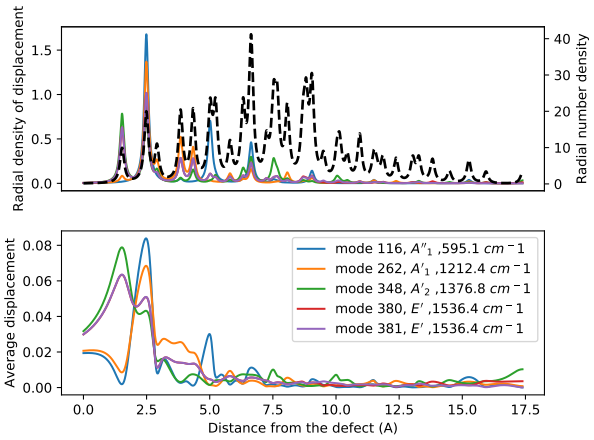

FIG. 6: The upper panel shows the radial density of displacement $d_\nu(r)$ as defined in Eq. 4 for the phonons with the highest localisation factor f^ν. The black dashed line indicates the radial number density. The lower panel represents the average displacement as defined in eq. 6.

modulus of the phonon eigenvector ξ_ν for the atoms up to the second nearest neighbors around the vacancy:

$$f^\nu = \sum_{i<=2^{nd}nn} |\xi^i_\nu|^2 \ . \tag{3}$$

The phonons modes with a localization factor higher than 50% are (in decreasing order of f^ν) ν=116, 262, 348, 380, 381. Their radial density of displacement

$$d_\nu(r) = \sum_i |\xi^i_\nu|^2 \delta(|\mathbf{r}_i - \mathbf{r}_{vac}|) \ , \tag{4}$$

the radial number density

$$n(r) = \sum_i \delta(|\mathbf{r}_i - \mathbf{r}_{vac}|) \ , \tag{5}$$

and the average density of displacement

$$d_\nu^{av}(r) = \frac{d_\nu(r)}{n(r)} \tag{6}$$

are represented in Fig. 6 (Here the index i refers to the atomic sites and $\mathbf{r}_{vac}$ is the vacancy position). It is easy to see that these very local phonon modes do not coincide with those dominating the exciton-phonon coupling spectrum of Fig. 2b of the main text, although the phonon mode $\nu = 120$ as a localization factor of 40.1%. Therefore we conclude that there is not a trivial relation between exciton-phonon coupling and the localization of the phonons around the vacancy. The phonon mode dominating the exciton-phonon coupling spectrum is $\nu = 120$. As shown in Fig. 7, it is charachterized by a out-of-plane displacement of the atoms around the vacancy, and is peaked in correspondence of the second nearest-neighbours boron atoms.

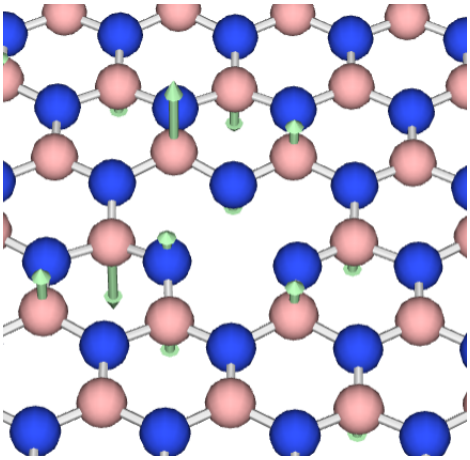

FIG. 7: Representation of the eigenvector of the phonon mode $\nu = 120$.

DIPOLE SELECTION RULES FOR D_{3h} AND C_{2v} GROUPS

The dipole matrix element between two states $|\psi_i\rangle$ and $|\psi_j\rangle$ is defined as:

$$\mathbf{d}_{ij} = \langle\psi_i|\hat{\mathbf{r}}|\psi_j\rangle \tag{7}$$

According to the selection rules from group theory [8], the dipole vanishes if the product of the irreducible representations of the wavefunctions $|\psi_{i/j}\rangle$ and the position operator $\hat{\mathbf{r}}$ does not contain the fully symmetric irreducible representation, which is labelled A_1' for the D_{3h} and A_1 for the C_{2v} one. The product tables for the D_{3h} and C_{2v} are reported in Tab. I and II respectively.

For the D_{3h} group, the in plane components (x,y) of $\hat{\mathbf{r}}$ transform as the irreducible representation E', while the out of plane component z as A_2''. Tab. III shows which dipoles matrix elements vanish for symmetry in the symmetric systems. For the C_{2v} group, the in plane components (x,y) of $\hat{\mathbf{r}}$ transform as the irreducible represenations (A_1, B_1), while the out of plane component z as B_2. Tab. IV shows which dipoles matrix elements vanish for symmetry in the Jahn-Teller distorted systems.

	$\mathbf{A_1'}$	$\mathbf{A_2'}$	$\mathbf{E'}$	$\mathbf{A_1''}$	$\mathbf{A_2''}$	$\mathbf{E''}$
$\mathbf{A_1'}$	A_1'	A_2'	E'	A_1''	A_2''	E''
$\mathbf{A_2'}$	A_2'	A_1'	E'	A_2''	A_1''	E''
$\mathbf{E'}$	E'	E'	$A_1' + A_2' + E'$	E''	E''	$A_1'' + A_2'' + E''$
$\mathbf{A_1''}$	A_1''	A_2''	E''	A_1'	A_2'	E'
$\mathbf{A_2''}$	A_2''	A_1''	E''	A_2'	A_1'	E'
$\mathbf{E''}$	E''	E''	$A_1'' + A_2'' + E''$	E'	E'	$A_1' + A_2' + E'$

Table I: Product table for the D_{3h} group.

	$\mathbf{A_1}$	$\mathbf{A_2}$	$\mathbf{B_1}$	$\mathbf{B_2}$
$\mathbf{A_1}$	A_1	A_2	B_1	B_2
$\mathbf{A_2}$	A_2	A_1	B_2	B_1
$\mathbf{B_1}$	B_1	B_2	A_1	A_2
$\mathbf{B_2}$	B_2	B_1	A_2	A_1

Table II: Product table for the C_{2v} group.

$\|\psi_i\rangle$	$\|\psi_j\rangle$	d_{xy}	d_z
A_2''	E'	0	0
E''	E'	0	$\neq 0$
E''	E'	0	$\neq 0$
A_1'	E'	$\neq 0$	0
A_2''	E''	$\neq 0$	0

Table III: Value of the dipole matrix elements for some transitions of interest in the symmetric system (D_{3h} group).

$\|\psi_i\rangle$	$\|\psi_j\rangle$	d_{xy}	d_z
B_2	B_1	0	0
B_2	A_1	0	$\neq 0$

Table IV: Value of the dipole matrix elements for some transitions of interest in the Jahn-Teller distorted system (C_{2v} group).

STATIC JAHN-TELLER DISTORTION

The doubly degenerate spin down excited state e' can undergo Jahn-Teller distortion, which reduces the symmetry group of the system from D_{3h} to C_{2v}. As a conquence of it, the doubly degenerate spin down acceptor e' splits into the levels a_1 and b_1, while the a_2'' level is turned into b_2 (as shown in Fig. 8). In order to study the Jahn-Teller distorted system, we perform DFT calculations where we relax the system while constraining the occupation of one of the e' orbitals to 1.0 and that of the orbital a_2'' to 0. As expected, we find two local minima, corresponding to the two possible configurations in which the doubly degenerate excited state is distorted. One of them has the level a_1 lying below the level b_1, while in the other this order is switched. In our occupation model, only the lowest lying empty level has a non negligible nonequilibrium population. Therefore, we consider the atomic configuration in which the a_1 level is the lowest (Fig. 8b), as the transition $a_1 \to b_2$ is allowed by symmetry while the transition $b_1 \to b_2$ is forbidden (see Tab. IV).

Since the Jahn-Teller distortion is small, we assume in a first approximation that the exciton energies and wavefunctions remain equal to those of the original symmetric system. The significative difference between the distorted and the symmetric systems is that now the transition $a_1 \to b_2$ ($e' \to a_2''$) is symmetry-allowed, and this affects the contribution of each exciton to the photoluminescence spectrum. Therefore, in order to check whether the Jahn-Teller effect could be the responsible of the activation of the peak at 1.5 eV, we compute the dipole matrix elements corresponding to the transitions $a_1 \to b_2$ and $b_1 \to b_2$ for the distorted system, and use these to recalculate the exciton contributions to photoluminescence.

As commented in the main text, the enhancement of the peak at 1.5 eV due to the static Jahn-Teller effect is very small. It is not difficult to understand the reason: the transition $a_1 \to b_2$ has a non-vanishing out-of-plane dipole that is very small due to the atomically thin material. In addition to this, the Jahn-Teller effect distorts only slightly the geometry, leading to an even weaker dipole moment for the transition.

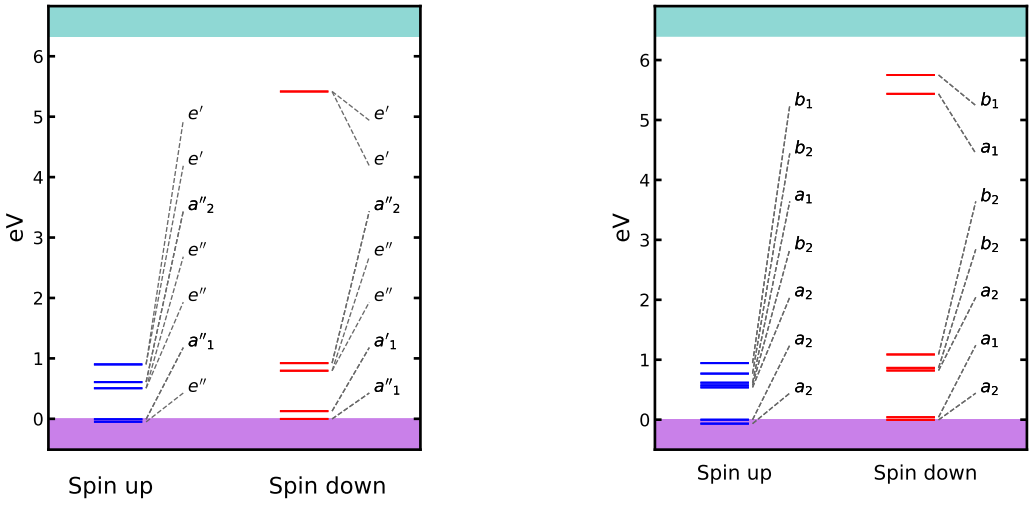

(a) Symmetric system

(b) Jahn-Teller distorted

FIG. 8: In panel (a) we replicate Fig. 5.a of the main text, showing the defect levels of the symmetric system calculated at G_0W_0 level of theory. This figure is proposed again here in order to allow a better comparison with the defect levels of the Jahn-Teller distorted system represented in panel (b).

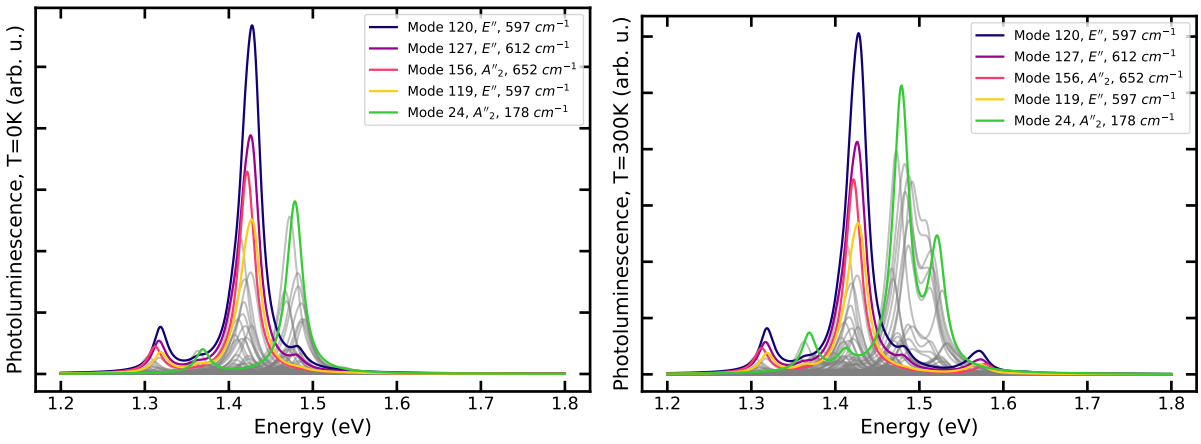

(a) T=0K (b) T=300K

FIG. 9: Contribution of each phonon to the luminescent emission at T=0K (panel a) and T=300K (panel b). The phonon modes which couple most strongly with excitons are enlightened with coloured lines while the other phonon modes are represented with grey lines.

If we plot the full contribution of each phonon to the luminescence (as defined in Eq. 2 of the main text), we can see that the factors $\frac{n_B(\omega_\nu,T)}{2\omega_\nu}$ and $\frac{n_B(\omega_\nu,T)+1}{2\omega_\nu}$, which multiply the phonon annihilation and the phonon creation peaks respectively, have two main effects. First of all, at low temperatures, the weight corresponding to the phonon creation tends to zero; therefore, only emission at energies lower than E_λ is expected: Fig. 9a shows a vanishing contribution to the emission for energies higher than 1.5 eV at T=0K, while it increases remarkably at T=300K. This growth in importance of the phonon creation term with the temperature leads to a broadening of the PL spectrum, as shown in Fig. 3 of the main paper. Furthermore, as the temperature increases, the low-energy phonons tend to contribute more than the high-energy ones. This can be observed by considering the increase in importance of mode $\nu = 24$ of frequency 178 cm^{-1} (green line), with respect to mode $\nu = 120$ of frequency 570 cm^{-1} (blue line), leading to the shift towards higher energies of the maximum of the photoluminescence spectrum, as seen in Fig. 3 of the main text.

COMPARISON WITH OTHER EXPERIMENTAL SPECTRA

The theoretical photoluminescence spectrum in Fig. 1 of the main paper has been compared with the experimental curve from Ref. [7], which, according to the authors, correspond to isolate emitters. The experimental spectrum of Ref. [9], instead, corresponds to an ensemble of spins, and is broader [7]. It is interesting to compare the theoretical results also with the spectrum of a non-identified defect in 3D hBN reported in Fig. 3b of Ref. [10], which is characterized by emission at ∼1.6 eV. Fig. 10 reports both this experimental spec-

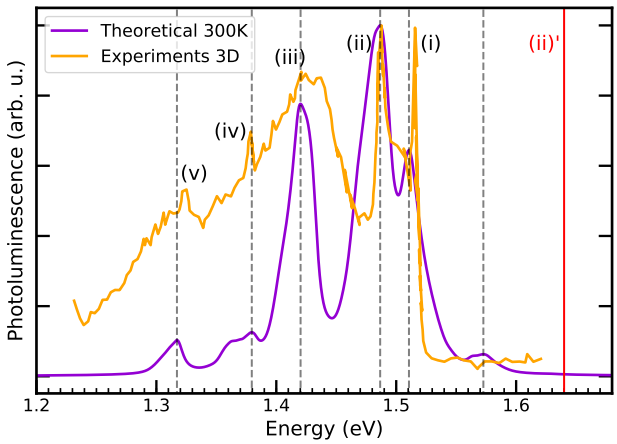

FIG. 10: Theoretically predicted photoluminescence spectrum for negatively charged boron vacancy in 2D hBN is compared with the experimental spectrum [10] of a non-identified defect in 3D hBN. The experimental spectrum is aligned with the theoretical one, in such a way that the second peak from the right coincide. The theoretical curve represents the very same spectrum as in Fig. 1 of the main paper, with the only difference that the artificial broadening adopted is very small in this case (0.005 eV, against the 0.04 eV of the figure in the main text) to enlighten the peaks corresponding to the most important phonons. The vertical red line (ii)' corresponds to the energy of the peak (ii) before the shift, and witness a very good agreement also in the absolute position of the theoretical and experimental spectra.

trum and the theoretical spectrum for V_B^- in 2D hBN. According to the authors of Ref. [10], the peak (i) of this experimental curve is probably due to the background, therefore the highest energy peak corresponding to the defect is the second (ii). The theoretical peak at 1.51 eV corresponds to the annihilation of low frequency phonons, and is weaker than that

at 1.49 eV, corresponding to the their creation. If we shift the experimental curve in such a way that the most intense peaks coincide (peak (ii) for the experiments and that at 1.49 eV for the theory), we observe a remarkable agreement in the position of the remaining peaks, i.e. (iii), (iv) and (v). In order to realize such alignment, it is necessary to redshift the experimental spectrum of 0.14 eV, witnessing a very good agreement also in the absolute position of the spectra. Basing on this agreement, we may conclude that:

1. the spectrum in Fig. 3b of Ref. [10] is the negatively charged boron vacancy in 3D hBN;

2. the peak (ii), which was tentatively associated to the ZPL by the authors, correspond instead to the first replica of a phonon of low frequency.

It must be stressed that an agreement between the spectra corresponding to the same defect in 3D and 2D hBN can be due to the following factors. First of all, the phonons for the 2D hBN look globally similar to those for the 3D hBN, with more marked differences for the LO modes in the long-wavelength limit [11]. However, as it can be seen in Fig. 9, the contribution of the high frequency phonons to photoluminescence is small. Furthermore the in-plane dipoles, which are those affecting the most the spectrum, are not likely to change significantly when passing from the 2D to the 3D structure.

COMPARISON WITH THE HUANG-RHYS METHOD

As anticipated in the main text, the most used technique for the calculation of the PL lineshape of defect centers in semiconductors is based on a generalization of the Huang-Rhys (HR) model [12]. This work assumes that the energy difference between ground and excited state depends on a fictitious coordinate ξ which is linear function of the ground state normal modes. The difference between the relaxed position of the atoms in the excited and in the ground state is thus expanded in term of normal modes to determine the modal coordinates [13]

$$q_k = \sum_{\alpha,i} m_\alpha^{1/2} (R^e_{\alpha i} - R^g_{\alpha i}) e^k_{\alpha i} \ , \tag{8}$$

which are later used to calculate the partial Huang-Rhys factor S_k measuring the coupling of the phonon k with the electrons:

$$S_k = \frac{\omega_k q_k^2}{2\hbar} \ . \tag{9}$$

Here α labels the atoms, i refers to the cartesian component, $R^{e/g}_{\alpha i}$ are the equilibrium positions of the atoms in the excited/ground state and $e^k_{\alpha i}$ is a normalized vector that describes the displacement of the atom α along the direction i in the phonon mode k, and ω_k is the phonon frequency. The function

$$S(t) = \int_0^\infty \sum_k S_k \delta(\hbar\omega - \hbar\omega_k) e^{-i\omega t} d(\hbar\omega) \tag{10}$$

is used to calculate the generating function

$$G(t) = e^{S(t) - S(0)} \tag{11}$$

(see Ref. [14] for a finite temperature treatment) whose Fourier transform is proportional to the PL lineshape:

$$L(E_{ZPL} - \hbar\omega) = \omega^3 \int_{-\infty}^{\infty} \frac{1}{2\pi} G(t) e^{i\omega t - \gamma|t|} dt \ . \tag{12}$$

Here γ is the broadening of the phonon peaks and E_{ZPL} is the zero-phonon line, which is determined through constrained DFT or quantum chemistry calculations. We now review the main limitations of this method and see how the many-body perturbation theory (MBPT) treatment of the PL presented in the main text manages to overcome them. First of all, the

starting point of the theory summarized above is the following expression for the absolute intensity of the emission [12, 13]:

$$I(\hbar\omega) = \frac{n_D \omega^3}{3\epsilon_0 \pi c^3 \hbar} \, |\mu_{eg}|^2 \sum_m |\, \langle \chi_{gm} | \chi_{e0} \rangle \,|^2 \, \delta(E_{ZPL} - E_{gm} - \omega\hbar) \;, \tag{13}$$

where n_D is the refractive index, and $|\mu_{eg}|$ is the optical dipole moment between ground and excited states. This formula is valid for molecules (in which case $n_D = 1$) or for solids with homogeneous and isotropic screening, but not for 2d materials, where the screening environment is more complex. In the theory presented in the main text, instead, the whole screening function is calculated through state-of-the-art MBPT calculations [3].

The main assumption behind the Huang-Rhys theory is that the optical dipole moment between ground and excited state $|\mu_{eg}|$ is not affected by phonons (Frank-Condon approximation). This allows to take $|\mu_{eg}|$ out of the summation in Eq. 13. As we will show later this assumption limits strongly the predictivity of the theory. In the many-body perturbation theory, instead phonon dependence of the optical dipole moments is correctly taken into account, as witnessed by the terms $\frac{\partial^2 |\Pi_\lambda|^2}{\partial x_\nu^2}$ in Eq. 2 of the main text.

As shown by Eq. 9, only the phonon modes with non-vanishing modal coordinate q_k contributes to the PL lineshape of the Huang-Rhys method. Now, both Refs. [7, 15] agree that the observed luminescence is associated to the transition between the many-body states $(1)^3E'' \rightarrow (1)^3A_2'$, which corresponds to the transition between the single particle states $e' \rightarrow a_2''$ of the main text. However, the relaxed geometry of the state $(1)^3E''$ remains flat even when considering the Jahn-Teller distortion (i.e. all the atoms have 0 displacement in the out-of-plane direction). This has the fundamental consequence that $q_k = 0$ for all the out-of-plane phonon modes: therefore, these modes do not contribute to the HR luminescence. The formalism presented in the main text is beyond the Franck-Condon approximation, and instead predicts that the out-of-plane phonon modes are those affecting most the photoluminescence. It is instructive to calculate the PL with the MBPT approach presented in the main text and excluding the contribution of the phonons of symmetry A_1'', A_2'' and E'' (i.e. those phonons which do not contribute to the PL in the Huang-Rhys method). The result is shown in violet dashed line in Fig. 11, and compared with the calculations of the PL through the HR method from Ref. [15] (represented in green solid line). In order to facilitate the comparison, the main peak of the two spectra has been aligned. The two spectra are perfectly superimposed in the interval of frequencies ranging from 1.6

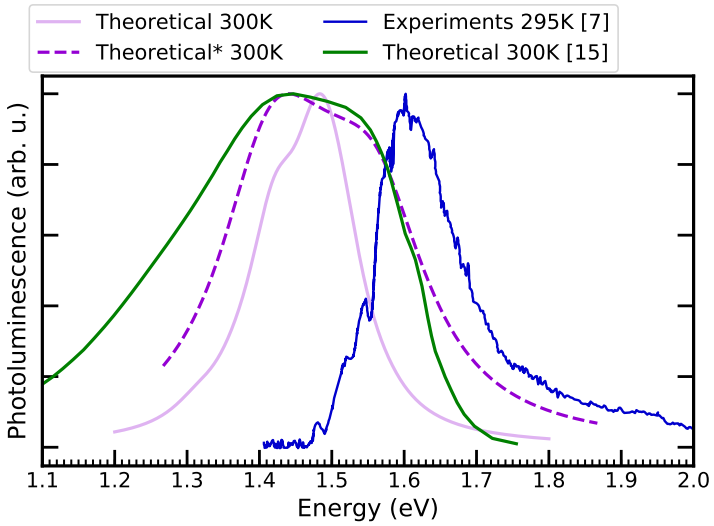

FIG. 11: The violet dashed line is obtained from the MBPT approach of the main text when excluding the contribution of the phonon modes of symmetry A_1'', A_2'' and E''. This curve is compared to the result from the HR method of Ref. [15], represented in green solid line. The former curve is shifted in such a way that the main peak coincide with that of the green curve. The solid violet line represents the PL calculated through the MBPT approach when including the contribution of all the phonons, while the solid blue curve represents the experimental PL from Ref. [7].

eV (where the ZPL of the HR calculation lies, as reported in [15]) to 1.4 eV (position of the main peak). The MBPT spectrum decays faster than the HR one for small frequencies, as it does not take into account the harmonic replica. In both cases, the spectrum is much broader than the experimental one [7], represented in solid blue line. The result is improved dramatically when the contribution of phonons of all the symmetries is considered when calculating the PL with the MBPT approach, leading to the curve represented in solid violet line (and reported in Fig. 1 of the main text). We thus conclude that the PL is dominated by the phonon modes which are odd with respect to the mirroring with the plane of the 2D material. This explains the failure of the HR method in reproducing the PL lineshape of the charged B vacancy.

Regarding the limitation of our method, it does not take into account the polaron shift and the presence of multi-phonon replica. The former can be calculated including also the electron-phonon diagrams in the perturbative series for the one particle and two particles

Green's function, while the latter can be determined through by expanding the theory presented in Ref. [16] to higher orders.

[1] P. Giannozzi, S. Baroni, N. Bonini, M. Calandra, R. Car, C. Cavazzoni, D. Ceresoli, G. L. Chiarotti, M. Cococcioni, I. Dabo, A. D. Corso, S. de Gironcoli, S. Fabris, G. Fratesi, R. Gebauer, U. Gerstmann, C. Gougoussis, A. Kokalj, M. Lazzeri, L. Martin-Samos, N. Marzari, F. Mauri, R. Mazzarello, S. Paolini, A. Pasquarello, L. Paulatto, C. Sbraccia, S. Scandolo, G. Sclauzero, A. P. Seitsonen, A. Smogunov, P. Umari, and R. M. Wentzcovitch, Journal of Physics: Condensed Matter **21**, 395502 (2009).

[2] M. van Setten, M. Giantomassi, E. Bousquet, M. Verstraete, D. Hamann, X. Gonze, and G.-M. Rignanese, Computer Physics Communications **226**, 39 (2018).

[3] A. Marini, C. Hogan, M. Grüning, and D. Varsano, Computer Physics Communications **180**, 1392 (2009).

[4] D. Sangalli, A. Ferretti, H. Miranda, C. Attaccalite, I. Marri, E. Cannuccia, P. Melo, M. Marsili, F. Paleari, A. Marrazzo, G. Prandini, P. Bonfà, M. O. Atambo, F. Affinito, M. Palummo, A. Molina-Sánchez, C. Hogan, M. Grüning, D. Varsano, and A. Marini, Journal of Physics: Condensed Matter **31**, 325902 (2019).

[5] A. Togo and I. Tanaka, Scr. Mater. **108**, 1 (2015).

[6] C. Attaccalite, M. Bockstedte, A. Marini, A. Rubio, and L. Wirtz, Phys. Rev. B **83**, 144115 (2011).

[7] J. R. Reimers, J. Shen, M. Kianinia, C. Bradac, I. Aharonovich, M. J. Ford, and P. Piecuch, Phys. Rev. B **102**, 144105 (2020).

[8] M. Tinkham, *Group Theory and Quantum Mechanics* (Dover Publications, 2003).

[9] A. Gottscholl, M. Kianinia, V. Soltamov, S. Orlinskii, G. Mamin, C. Bradac, C. Kasper, K. Krambrock, A. Sperlich, M. Toth, I. Aharonovich, and V. Dyakonov, Nature Materials (2020).

[10] T. T. Tran, C. Zachreson, A. M. Berhane, K. Bray, R. G. Sandstrom, L. H. Li, T. Taniguchi, K. Watanabe, I. Aharonovich, and M. Toth, Phys. Rev. Applied **5**, 034005 (2016).

[11] T. Sohier, M. Gibertini, M. Calandra, F. Mauri, and N. Marzari, Nano Letters **17**, 3758 (2017).

[12] M. Lax, The Journal of Chemical Physics **20**, 1752 (1952), https://doi.org/10.1063/1.1700283.

[13] A. Alkauskas, B. B. Buckley, D. D. Awschalom, and C. G. V. de Walle, **16**, 073026 (2014).

[14] Y. Jin, M. Govoni, G. Wolfowicz, S. E. Sullivan, F. J. Heremans, D. D. Awschalom, and G. Galli, Physical Review Materials **5** (2021), 10.1103/physrevmaterials.5.084603.

[15] V. Ivády, G. Barcza, G. Thiering, S. Li, H. Hamdi, J.-P. Chou, Ö. Legeza, and A. Gali, npj Computational Materials **6**, 41 (2020).

[16] E. Cannuccia, B. Monserrat, and C. Attaccalite, Phys. Rev. B **99**, 081109 (2019).